



OPEN

SUBJECT AREAS:
NANOSCALE MATERIALS
NANOSCALE DEVICESReceived
25 September 2013Accepted
26 November 2013Published
16 December 2013Correspondence and
requests for materials
should be addressed to
J.M.M.
(nanoelechem@hnu.
edu.cn); Z.X.
(patrick_xuyang@
163.com) or T.H.W.
(thwang@hnu.edu.cn)

Hierarchical SnO₂ Nanospheres: Bio-inspired Mineralization, Vulcanization, Oxidation Techniques, and the Application for NO Sensors

Lei Wang, Yuejiao Chen, Jianmin Ma, Libao Chen, Zhi Xu & Taihong Wang

Key Laboratory for Micro-Nano Optoelectronic Devices of Ministry of Education, State Key Laboratory for Chemo/Biosensing and Chemometrics, Hunan University, Changsha, 410082, P. R. China.

Controllable synthesis and surface engineering of nanomaterials are of strategic importance for tailoring their properties. Here, we demonstrate that the synthesis and surface adjustment of highly stable hierarchical of SnO₂ nanospheres can be realized by biomineralization, vulcanization and oxidation techniques. Furthermore, we reveal that the highly stable hierarchical SnO₂ nanospheres ensure a remarkable sensitivity towards NO gas with fast response and recovery due to their high crystallinity and special structure. Such technique acquiring highly stable hierarchical SnO₂ nanospheres offers promising potential for future practical applications in monitoring the emission from waste incinerators and combustion process of fossil fuels.

Rational design and control over the morphology and the functional properties of inorganic nanostructures have been a long-standing subject in the development of bottom-up device fabrication processes¹. In the past decade, tin oxide (SnO₂) has been extensively applied in the fields of lithium-ion batteries (LIBs), gas sensors, light-emitting diodes (LEDs), solar cell, catalysis and so on owing to its excellent electrical and optical properties^{2–6}. These properties are usually strongly dependent on SnO₂ nanostructures. Thus, tremendous effort has been focused on the synthesis of SnO₂ nanostructures such as nanocrystals (NCs)⁷, nanoboxes², nanorods (NRs)⁸, nanowires (NWs)⁹, nanobelts (NBs)¹⁰, nanoplates (NPs)¹¹, hollow nanospheres (HNSs)¹², nanorod-bundles (NRBs)¹³, etc. Although many sophisticated synthetic methods have been developed so far, it is still a challenge to manipulate or adjust the structure and morphology of SnO₂ nanostructures.

Bio-inspired mineralization has been proved to be an innovative strategy to the fabrication of functional crystals with complex forms which mimic nature¹⁴, and has been expanded to the design and preparation of nonbiological minerals¹⁵. In recent years, some pioneering research on the synthesis of many functional materials or their precursors employing the bio-inspired mineralization methods has been reported^{16–21}. For example, Wu et al. synthesized the calcite superstructures with two different platonic shapes (pseudo-dodecahedral and pseudo-octahedral structures) by a polymer-controlled crystallization method via a cooperative assembly process of primary nanocrystals and mesocrystal formation¹⁶. Rana and his coworkers reported a polyamine-mediated bio-inspired synthesis methodology for preparing Ag/AgCl/ZnO composite materials with enhanced photocatalytic activity in a single step at room temperature and neutral pH²⁰. Recently, Yu group synthesized the hierarchical FeOOH nanostructure array films constructed by different nanosized building blocks at the air-water interface via a bio-inspired gas-liquid diffusion method²¹. These excellent results inspire us to explore new bio-inspired mineralization route to synthesize SnO₂ with some promising properties. In addition, in regard of bio-inspired synthesis of SnO₂, several interesting work also have been conducted. Su and co-workers successfully used biomolecules in pollen coats to guide the self-assembly of SnO₂-precursors²², and also fabricated the interwoven tubular hierarchy of SnO₂ films using a biotemplate eggshell membrane combined sol-gel approach²³. More recently, Tremel group employed a surface-bound spermine to promote the fast deposition of homogeneous, thin and transparent biomimetic SnO₂ coatings on glass surfaces with high photoactivity²⁴. These reports urgently drive us to develop a mild, facile, and environmentally benign approach to prepare SnO₂ crystals with specific morphologies and nanostructures that will endow them with larger scale applications.



Structural manipulation of nanocrystals has been of significant interest as a way to tune their properties for enhanced performance in various applications^{25–29}. To date, some methods have been used to change the surface properties of nanocrystals, such as sub-structure, composites, surface ligand exchange, et al.^{25–32}. For example, Lou et al. reported that α -Fe₂O₃ microboxes with hierarchically structured shells can be synthesized simply by annealing Prussian blue (PB) microcubes at different temperatures²⁵. Tessler group demonstrated tuning of the electronic level positions with respect to the vacuum level in colloidal InAs nanocrystals using surface ligand exchange²⁶. Jasieniak and Mulvaney used the successive ion layer adhesion and reaction (SILAR) protocol to manipulate the surface stoichiometry of CdSe NCs from Cd-rich to Se-rich²⁷. These interesting results encourage us to look for new techniques to manipulate the surface of SnO₂ crystals for obtaining enhanced properties. For the modification of SnO₂ surfaces, there also exist some reported examples. For example, Zhang et al. synthesized the SnS₂/SnO₂ nanocomposites with tunable SnO₂ contents via in situ hydrothermal oxidation of SnS₂ nanoparticles in 0.375–4.5 mass% H₂O₂ aqueous solutions at 180°C for 0–12 h³⁰. Chen group reported that carbon-coated SnO₂ hollow microspheres synthesized with the assistance of d-glucose demonstrated higher reversible capacity and good cycling performance than that of pure SnO₂³¹. Kim and his co-workers reported Bimetallic Pd/Pt nanoparticles functionalized networked SnO₂ nanowires via a sequential γ -ray radiolysis can obtain a fast response and recovery ability in their NO₂-sensing performance³². Therefore, it is very meaningful to tune the properties of SnO₂ nanostructures via an effective structure manipulation.

Herein, we report a facile, green biomineralization process to synthesize stable hierarchical SnO₂ nanospheres (SnO₂ HNSs-1) using bio-inspired hydrothermal method with the assistance of tris(hydroxymethyl) aminomethane (THAM). The structure and composition of the as-obtained SnO₂ nanospheres can be further adjusted by vulcanization and oxidation techniques, after which the hierarchical S-doped SnO₂ nanospheres (SnO₂ HNSs-2) and novel hierarchical SnO₂ nanospheres (SnO₂ HNSs-3) can be easily produced, respectively. Structural characterizations were undertaken to investigate the correlation between the effects of biomineralization, vulcanization as well as oxidation processes on the structures and composition of the SnO₂ HNSs. Notably, gas sensors based on such stable SnO₂ HNSs exhibit the higher sensitivity towards NO gas with fast response and recovery. It is expected that the as-prepared SnO₂ HNSs-3 are promisingly applied to monitor the NO gas emission from waste incinerators and combustion process of fossil fuels.

Results

We have synthesized the three SnO₂ HNSs with different BET surface area and pore size using biomineralization, vulcanization and oxidation techniques. Firstly, we synthesized the stable SnO₂ HNSs-1 using bio-inspired hydrothermal method in the presence of THAM. Then, the as-synthesized SnO₂ HNSs-1 was modified by vulcanization method with TAA, and converted into the hierarchical S-doped SnO₂ nanospheres (SnO₂ HNSs-2). The as-obtained SnO₂ HNSs-2 was further oxidized in air at 500°C, and converted into the SnO₂ HNSs-3. The phase and structures of the three SnO₂ samples were characterized by X-ray powder diffraction (XRD). As shown in Figure 1, all of the diffraction peaks in the patterns for all the samples can be indexed to the tetragonal phase of SnO₂ (JCPDS no. 41-1445; $a = 0.47$ nm, $c = 0.32$ nm), and the broad nature of the XRD peaks indicates the presence of very small crystallites of SnO₂. Notably, there is no SnS₂ peak in the XRD pattern for SnO₂ HNSs-2, which may be due to the low content or low crystalline of SnS₂ in the SnO₂ HNSs-2. Energy dispersive X-ray spectroscopy (EDS) results (Figure S1a and b) confirm that there is the existence of a low amount of sulfur element in the SnO₂ HNSs-2 (S, w 0.2%) and not any sulfur element in the SnO₂ HNSs-3, respectively.

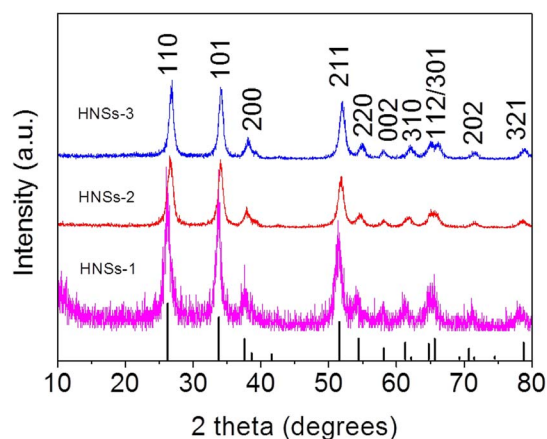


Figure 1 | XRD patterns for the three SnO₂ HNSs.

Transmission electron microscope (TEM) images show the morphology and structural analysis of the three SnO₂ HNSs (Figure 2). Figure 2a, d and g show the low-magnification TEM images of the SnO₂ HNSs-1, SnO₂ HNSs-2 and SnO₂ HNSs-3, respectively. In Figure 1a, d and g, one can find that all the three samples are well dispersed, without any aggregation, and they have a similar diameter of about 40 nm. In the high TEM images of SnO₂ HNSs (Figure 2b, e and h), they clearly show that interparticle distance of the SnO₂ HNSs-2 is largest among the three samples. This is proved to be effective for us to tailor the microstructures with the vulcanization technique. To further investigate the higher resolution TEM images in Figure 2c, f and i, we found that the nanoparticles of the SnO₂ HNSs increased and nanoparticles of the SnO₂ HNSs-3 were biggest after the vulcanization and oxidation treatments. It gives a clear proof for the effectiveness of our methods of structural control over the hierarchical SnO₂ nanospheres. Moreover, the textural properties of the SnO₂ HNSs were further investigated by measuring adsorption-desorption isotherms of nitrogen at 77 K, as shown in Figure S2. The Brunauer–Emmett–Teller (BET) specific surface areas (S_{BET}) for the SnO₂ HNSs-1, SnO₂ HNSs-2 and SnO₂ HNSs-3 are 24, 72.3 and 35.6 m²/g, respectively. Moreover, their pore size distributions have also been changed largely. These results further confirm the important effects of the vulcanization and oxidation treatments on the structures of the SnO₂ HNSs.

The composition and elemental distribution of the as-synthesized SnO₂ HNSs-2 were further mapped through EDS by displaying the integrated intensity of oxygen, tin and sulfur signals as a function of the beam position when operating the TEM in scanning mode (STEM). An HAADF-STEM image of the SnO₂ HNSs-2 is shown in Figure 3a, which reveals the sample is almost monodisperse. The results shown in Figure 3b–d reveal that the three elements of O, Sn, and S are distributed very homogeneously in nanospheres and exhibit no apparent element separation or aggregation. Moreover, the Sn/S ratio measured from several nanospheres with EDS analysis show an average ratio of 70.96:0.24. This ratio is extremely high, similar to EDS results from SEM. It indicates that the content of S is relatively low in the SnO₂ HNSs-2.

Prompted by the porous appearance of SnO₂ HNSs, we believed that these SnO₂ HNSs must have potentially excellent gas-sensing performance as other sensing materials. NO gas is well-known as a highly toxic gas emitted from vehicles and industrial processes, thus it has become a studied target for semiconductor sensors. Thus, we studied the NO-sensing performance of the SnO₂ HNSs-1 and SnO₂ HNSs-3 (SnO₂ HNSs-2 is not good sensing material due to the existence of sulfur, which has been proved). The optimized working temperature was first confirmed by the following experiments. We have screened the sensitivity-temperature profile of two SnO₂ sensors from 25 to 300°C, and found that the highest sensitivity towards

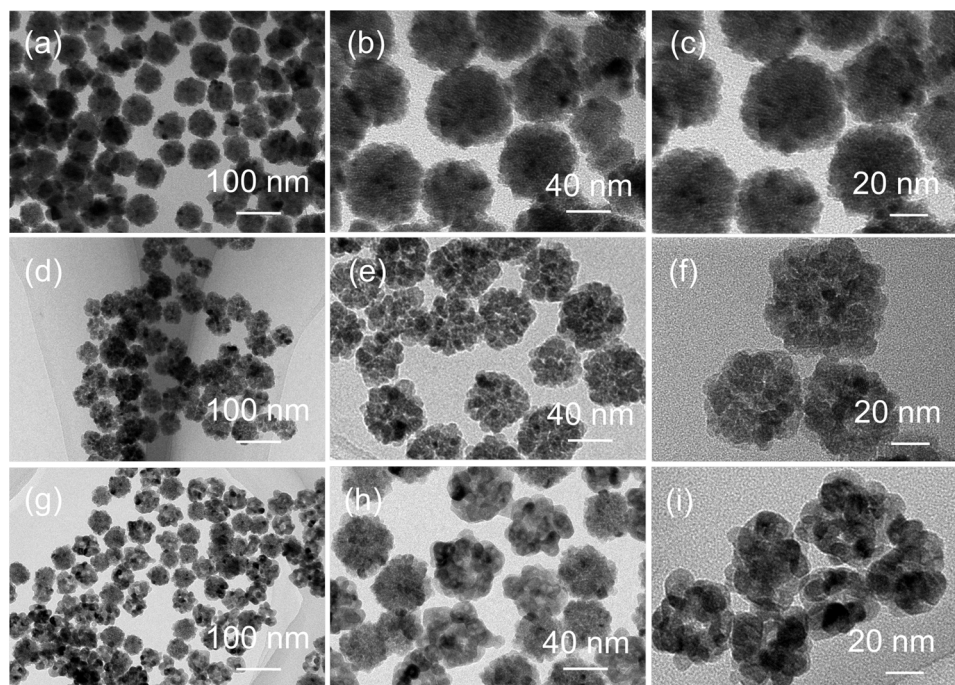


Figure 2 | TEM images for the three SnO₂ HNSs. (a–c) SnO₂ HNSs-1; (d–f) SnO₂ HNSs-2; (g–i) SnO₂ HNSs-3.

10 ppm NO gas for both of SnO₂ sensors could be obtained at 200°C, as shown in Figure 4a. The sensitivity of SnO₂ HNSs-3 is obviously superior to that of SnO₂ HNSs-1. Figure 4b further shows the response and recovery-time profiles of SnO₂ sensors towards 10 ppm NO gas, respectively. In Figure 4b, one can find that the response and recovery time of SnO₂ sensors become short when the temperature increases. Although the sensitivity of SnO₂ HNSs-3 is higher, its response and recovery is slower than these of SnO₂ HNSs-1. The response and recovery times of SnO₂ HNSs-3 are about 60 and 15 s, respectively. These data is better than those in reported sensor based on SnO_x-SWNT composite nanowires³³. Considering the above factors, thus, in the following section the optimal operating temperature for maximizing NO gas sensitivity was set at 200°C for further sensing analysis.

To investigate the response towards the various NO gas concentrations, the real-time response experiment was conducted. Figure 4c shows the real-time response and recovery curves of the three sensing materials (SnO₂ HNSs-1, SnO₂ HNSs-3 and commercial SnO₂ (c-SnO₂)) for the NO gas concentrations from 1 ppm to 100 ppm. In Figure 4c, one can find that the sensitivities for three SnO₂ sensors increase with NO gas concentrations increasing. However, the response increase for SnO₂ HNSs-1 and c-SnO₂ is extremely slow, which may be attributed to easy saturation to NO gas, and thus it limits the testing range. It also indicates that SnO₂ HNSs-3 has a strong response to NO gas in a wide range. In Figure 4d, the sensitivities of SnO₂ HNSs-3 sensor are shown to be also higher than that of SnO₂ HNSs-1 sensor, and increase with the NO concentration increasing from 1 ppm to 100 ppm. The sensitivities of SnO₂ HNSs-3 sensor towards 1, 10 and 100 ppm NO gas are about 14, 557 and 1147, respectively. The sensitivity of SnO₂ HNSs-3 sensor can be comparable to those of the reported NO sensors^{34,35}. Finally, we studied the gas-selectivity of the SnO₂ HNSs sensors through comparing the sensitivities towards various gases with the concentration of 10 ppm (Figure 4e). Figure 4e clearly shows that both of two SnO₂ HNSs sensors have higher sensitivities towards NO gas than the reducing gases (H₂S, CH₄, H₂ and CO). Due to its high sensitivity and selectivity, the SnO₂ HNSs-3 sensor is promising to be used to detect NO gas in future.

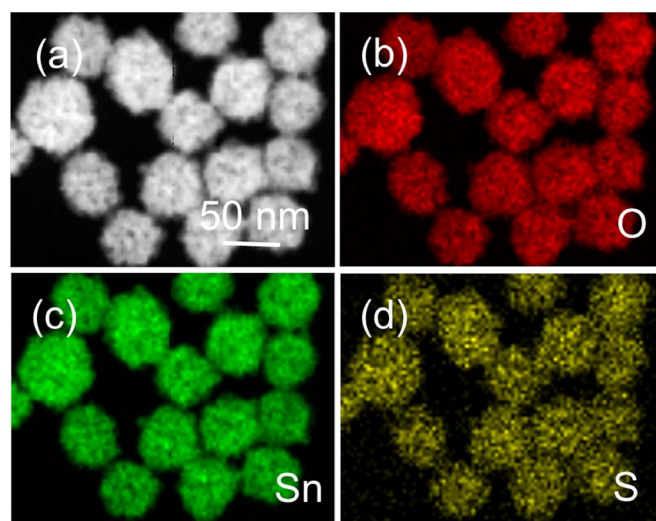


Figure 3 | STEM-EDS elemental maps of the SnO₂ HNSs-2. (a) HAADF-STEM image, (b) O elemental map, (c) Sn elemental map, and (d) S elemental map.

Discussion

The above-mentioned methods are very effective for us to adjust the microstructures and porous characteristics of the SnO₂ HNSs. In this work, some interesting chemical reactions were involved in the synthetic processes. The chemical processes are composed of the liquid-liquid, liquid-solid and gas-solid phase reactions. For the liquid-liquid phase reaction, Sn⁴⁺ ions were firstly hydrolyzed into SnO₂ in aqueous solution with THAM, which plays the important role in the formation of SnO₂ HNSs assembled by small nanocrystals as a mineralizer (see Figure S3 in the SI); for the solid-liquid phase reaction, SnO₂ were partly vulcanized into S-doped SnO₂ in aqueous solution with TAA; for the gas-solid phase reaction, the S-doped SnO₂ HNSs were further oxidized to SnO₂ by oxygen in air at

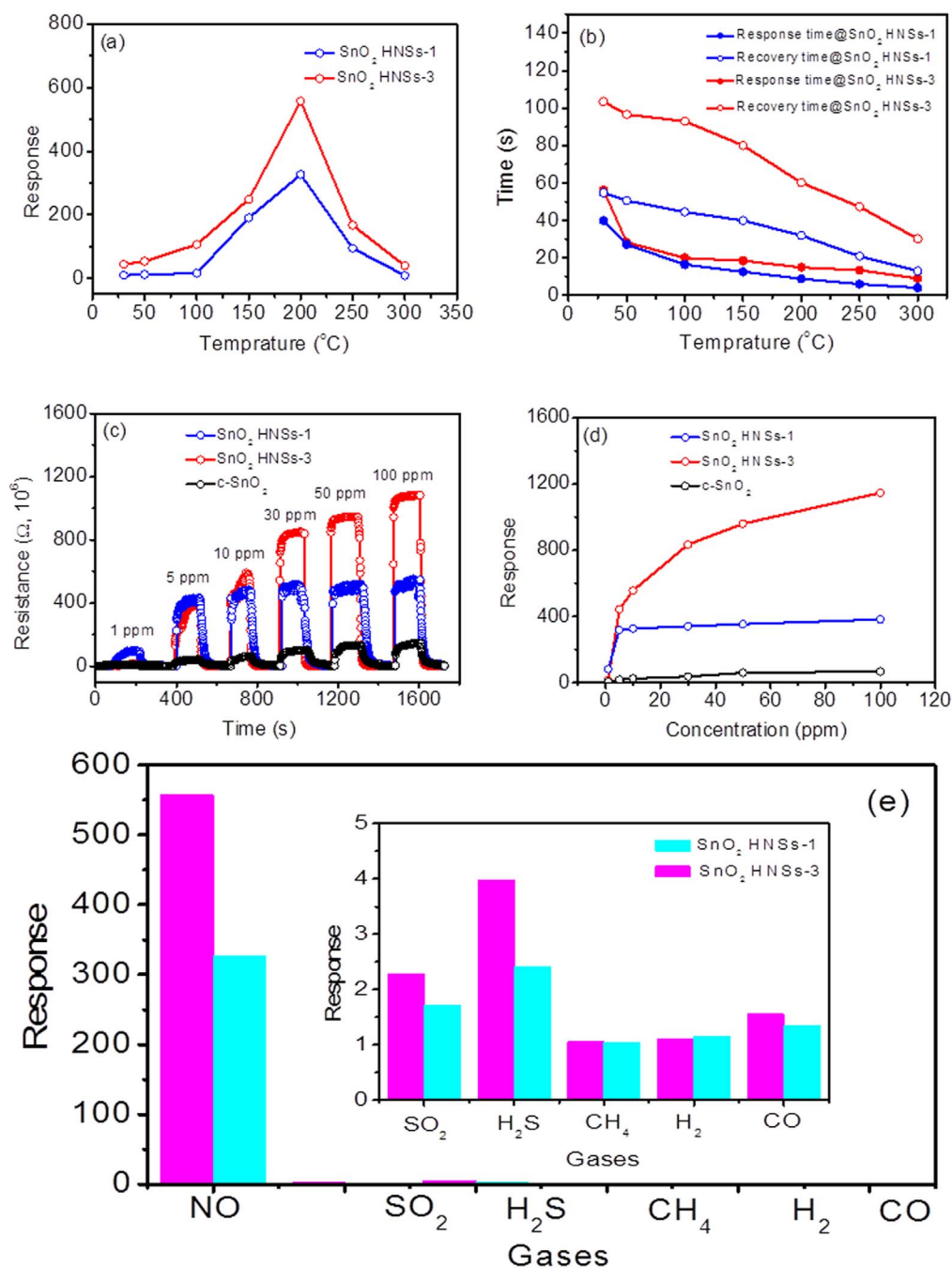


Figure 4 | Gas-sensing performance for the SnO₂ HNSs-1 and HNSs-3. (a) sensitivity and (b) response and recovery time of two sensors to 10 ppm NO gas at different working temperature; (c) The real-time response curve of three sensors to NO gas with increased concentration at a working temperature of 200°C; (d) The relationship between the sensitivity and the NO concentration; (e) Sensor response to various gases with 10 ppm at 200°C.

500°C. Moreover, with the above-mentioned reactions, two important processes should be emphasized to illustrate us the crystal growth processes and microstructure change of SnO₂ HNSs. One is the Ostwald ripening process, during which SnO₂ nanospheres were formed in the assistance of THAM, and S-doped SnO₂ was formed with the vulcanization of SnO₂. Another is the recrystallization process, during which S-doped SnO₂ was completely oxidized into SnO₂ at high temperature. Due to the effective influence of above-mentioned processes, these methods should be extended to adjust the structure and composite of other materials for optimizing their properties or performance.

The SnO₂ HNSs-3 sensor displays fast response and recovery as well as high sensitivity towards NO gas. Therefore, it is necessary to

research the NO-sensing mechanism of SnO₂ HNSs and analyze the potential reasons. It is widely reported that the change in resistance for SnO₂-based sensors is mainly caused by the adsorption and desorption of gas molecules on the surface of the sensing structure⁹. It is well-known that tin oxide is an n-type semiconductor originating from the oxygen vacancy in the non-stoichiometric SnO_x. When NO gas is adsorbed on the surface of SnO_x as an oxidizing molecule, capturing electrons from SnO_x, and thus, the consequent decrease in the number of electrons in SnO_x causes an increase of resistance of the sensors³³. Epifani and coauthors suggested that the bridging vacancies, generated by heat treatment at 500°C, can enhance the charge transfer from the surface to the adsorbate³⁶. Another model of the significant electron transfer to the adatoms



suggested by Maiti et al. can also well explain an orders-of-magnitude drop in electrical conductance for the oxidizing gas (NO)³⁷. For the sensors described here, we believe that the high sensitivity towards NO gas can be attributed to the intrinsically small grain size and high surface-to-volume ratios associated with the hierarchical nanospheres⁹. The network of interconnected pores in the sensor facilitates both the analyte and the background gas to access all the surfaces of SnO₂ nanoparticles contained in the sensing unit. Due to the unique porous structure and high S_{BET} of SnO₂ HNSs-3, more NO gas could be adsorbed onto the semiconductor surface, where subsequent reaction with surface oxygen species ($\text{O}_{2\text{ads}}^-$) causes the reduction in the electron concentration, resulting in the obvious increase in the sensor resistance^{33,34}. Therefore, the excellent response of SnO₂ HNSs-3 to NO gas could be attributable to the unique porous structure and high S_{BET} , for facilitating the electron transfer onto the surface of SnO₂ nanoparticles.

In summary, we have successfully synthesized, and adjusted the structure and composition of hierarchical SnO₂ nanospheres through biomineralization, vulcanization and oxidation processes, respectively. The control over the structure and composite of nanospheres was found to be largely influence its gas-sensing properties and performance through changing the porous characteristics and composition. The as-tailored SnO₂ nanospheres have presented excellent performance towards NO gas and found the potential application of detecting automobile exhaust. We hope that our findings will pave the way for tailored design of other complicated gas-sensing materials in sensors.

Methods

Materials. All the reagents for synthesis and preparation were of analytic grade and used as received without further purification. $\text{Na}_2\text{SnO}_3 \cdot 3\text{H}_2\text{O}$ and TAA were purchased from Aldrich. THAM was provided by Beijing Chemical Factory.

Biomaterialization of highly stable hierarchical SnO₂ nanospheres. In a typical biomineralization process, 0.27 g of $\text{Na}_2\text{SnO}_3 \cdot 3\text{H}_2\text{O}$ and 0.2 g of THAM were first dissolved into 35 ml of distilled H₂O, and then transferred into a 40 mL Teflon-lined stainless-steel autoclave at 120 °C for 10 h. Finally, the obtained white sample was rinsed with deionized water, pure ethanol and dried in ambient conditions. In order to investigate the effect of THAM on the morphology of final products, a series of controlled experiments were also conducted, and the amount of THAM is 0, 0.05 and 0.5 g, respectively.

Slight vulcanization of hierarchical SnO₂ nanospheres and its oxidation. In order to vulcanize the as-synthesized SnO₂ nanospheres and further oxidize it, we carried the experiment as followings: Typically, 0.05 g of the as-synthesized SnO₂ nanospheres and 0.025 g of thioacetamide (TAA) were first dissolved into 35 ml of distilled H₂O, and then transferred into a 40 mL Teflon-lined stainless-steel autoclave at 180 °C for 10 h. Finally, the obtained yellow sample was rinsed with deionized water, pure ethanol and dried in ambient conditions. The as-obtained yell sample was calcined in air at 500 °C.

Characterization. The morphology and structural characteristics were observed using X-ray diffraction (XRD, Rigaku D/max 2500 diffractometer), high-resolution transmission electron microscopy (HRTEM, JEOL 2010), nitrogen adsorption-desorption isotherms (ASAP 2020 nitrogen adsorption apparatus) and high-angle annular dark field scanning TEM (HAADF-STEM) images (JEOL JEM-2100F electron microscope). The Brunauer-Emmett-Teller (BET) specific surface areas (S_{BET}) were calculated using the BET equation. Desorption isotherm was used to determine the pore size distribution using the Barret-Joyner-Halender (BJH) method.

Sensor measurements. The fabrication and testing principles of the gas sensor are similar to that described in our previous reports. Firstly, the SnO₂ samples were mixed with terpeneol to form a paste and then coated onto the outside surface of an alumina tube with a diameter of 1 mm and a length of 5 mm. A platinum coil through the tube was employed as a heater to control the operating temperature. To improve their stability and repeatability, the gas sensors were aged at 300 °C for 10 h in air. Here, the sensing properties of the sensors were measured by a NS-4003 series gas-sensing measurement system (China Zhong-Ke Micro-nano IOT, Internet of Things, Ltd.). The relative humidity (RH) is about 45%. The response and recovery times were defined as the time required for a change of the resistance to reach 90% of the equilibrium value after injecting and that for removing the detected gas, respectively. When air and ppm-level target gas were flowed through the sensor element, the corresponding steady-state resistances of the sensor in air (R_{air}) and in the air-gas

mixture (R_{gas}) were recorded, respectively. The sensor gas response for oxidizing gas (NO) is defined as the ratio of $R_{\text{gas}}/R_{\text{air}}$, while the response for reducing gas (H₂S, H₂, CO or CH₄) is defined as the ratio of $R_{\text{air}}/R_{\text{gas}}$ ³⁸.

- Joo, J. *et al.* Face-selective electrostatic control of hydrothermal zinc oxide nanowire synthesis. *Nature Mater.* **10**, 596–601 (2011).
- Wang, Z. Y. *et al.* Fast formation of SnO₂ nanoboxes with enhanced lithium storage capability. *J. Am. Chem. Soc.* **133**, 4738–4741 (2011).
- Wang, B. *et al.* Fabrication of a SnO₂ nanowire gas sensor and sensor performance for hydrogen. *J. Phys. Chem. C* **112**, 6643–6647 (2008).
- Li, Y. F. *et al.* Realizing a SnO₂-based ultraviolet light-emitting diode via breaking the dipole-forbidden rule. *NPG Asia Mater.* **4**, e30 (2012).
- Birkel, A. *et al.* Highly efficient and stable dye-sensitized solar cells based on SnO₂ nanocrystals prepared by microwave-assisted synthesis. *Energy Environ. Sci.* **5**, 5392–5400 (2012).
- Liu, G. B. *et al.* Selective oxidation of dimethyl ether to methyl formate over trifunctional MoO₃-SnO₂ catalyst under mild conditions. *Green Chem.* **15**, 1501–1504 (2013).
- Chen, Y. J. *et al.* Gram-scale synthesis of ultrasmall SnO₂ nanocrystals with an excellent electrochemical performance. *Nanoscale* **5**, 3262–3265 (2013).
- Xi, G. C. & Ye, J. H. Ultrathin SnO₂ nanorods: template- and surfactant-free solution phase synthesis, growth mechanism, optical, gas-sensing, and surface adsorption properties. *Inorg. Chem.* **49**, 2302–2309 (2011).
- Wang, Y. L. *et al.* A solution-phase, precursor route to polycrystalline SnO₂ nanowires that can be used for gas sensing under ambient conditions. *J. Am. Chem. Soc.* **125**, 16176–16177 (2003).
- Kolmakov, A. *et al.* Enhanced gas sensing by individual SnO₂ nanowires and nanobelts functionalized with Pd catalyst particles. *Nano Lett.* **5**, 667–673 (2004).
- Wang, C. *et al.* Large-scale synthesis of SnO₂ nanosheets with high lithium storage capacity. *J. Am. Chem. Soc.* **132**, 46–47 (2010).
- Lou, X. W. *et al.* Preparation of SnO₂/carbon composite hollow spheres and their lithium storage properties. *Chem. Mater.* **20**, 6562–6566 (2008).
- Wang, Q. H. *et al.* Shape-controlled synthesis of porous SnO₂ nanostructures via morphological conserved transformation from SnC₂O₄ precursor approach. *Nano-Micro Lett.* **3**, 34–42 (2011).
- Aizenberg, J. New nanofabrication strategies: Inspired by biomineralization. *MRS Bull.* **35**, 323–330 (2010).
- Kim, S. J. & Park, C. B. Bio-inspired synthesis of minerals for energy, environment, and medicinal Applications. *Adv. Funct. Mater.* **23**, 10–25 (2013).
- Song, R. Q. *et al.* Calcite crystals with platonic shapes and minimal Surfaces. *Angew. Chem. Int. Ed.* **48**, 395–399 (2009).
- Tao, A. R. *et al.* Bio-inspired nanofabrication of barium titanate. *J. Mater. Chem.* **20**, 7916–7923 (2010).
- Kim, Y. Y. *et al.* Bio-inspired synthesis and mechanical properties of calcite-polymer particle composites. *Adv. Mater.* **22**, 2082–2086 (2010).
- Xiao, J. W. & Yang, S. H. Biomimetic synthesis, hierarchical assembly and mechanical properties of calcite/chitosan composites in a three-dimensional chitosan scaffold. *Adv. Eng. Mater.* **13**, B32–B40 (2011).
- Begum, G. *et al.* Controlled orientation in a bio-inspired assembly of Ag/AgCl/ZnO nanostructures enables enhancement in visible-light-induced photocatalytic performance. *Chem. Eur. J.* **18**, 6847–6853 (2012).
- Liu, L. *et al.* Bio-inspired fabrication of hierarchical FeOOH nanostructure array films at the air-water interface, their hydrophobicity and application for water treatment. *ACS Nano* **7**, 1368–1378 (2013).
- Song, F. *et al.* 3D hierarchical porous SnO₂ derived from self-assembled biological systems for superior gas sensing application. *J. Mater. Chem.* **22**, 1121–1126 (2012).
- Dong, Q. *et al.* Fabrication and gas sensitivity of SnO₂ hierarchical films with interwoven tubular conformation by a biotemplate-directed sol-gel technique. *Nanotechnology* **17**, 3968–3972 (2006).
- André, R. *et al.* Self-cleaning antimicrobial surfaces by bio-enabled growth of SnO₂ coatings on glass. *Nanoscale* **5**, 3447–3456 (2013).
- Zhang, L. *et al.* Formation of Fe₂O₃ microboxes with hierarchical shell structures from metal organic frameworks and their lithium storage properties. *J. Am. Chem. Soc.* **134**, 17388–17391 (2012).
- Soreni-Harari, M. *et al.* Tuning energetic levels in nanocrystal quantum dots through surface manipulations. *Nano Lett.* **8**, 678–684 (2008).
- Jasieniak, J. & Mulvaney, P. From Cd-rich to Se-rich - the manipulation of CdSe nanocrystal surface stoichiometry. *J. Am. Chem. Soc.* **129**, 2841–2848 (2007).
- Yu, W. W. *et al.* Forming biocompatible and nonaggregated nanocrystals in water using amphiphilic polymers. *J. Am. Chem. Soc.* **129**, 2871–2879 (2007).
- Rivesta, J. B. & Jain, P. K. Cation exchange on the nanoscale: an emerging technique for new material synthesis, device fabrication, and chemical sensing. *Chem. Soc. Rev.* **42**, 89–96 (2013).
- Zhang, Y. C. *et al.* High-performance visible-light-driven SnS₂/SnO₂ nanocomposite photocatalyst prepared via in situ hydrothermal oxidation of SnS₂ nanoparticles. *ACS Appl. Mater. Interfaces* **3**, 1528–1537 (2011).
- Guo, X. W. *et al.* Lithium storage in carbon-coated SnO₂ by conversion reaction. *J. Power Sources* **226**, 75–81 (2013).
- Choi, S. W. *et al.* Bimetallic Pd/Pt nanoparticle-functionalized SnO₂ nanowires for fast response and recovery to NO₂. *Sensor. Actuat. B-Chem.* **181**, 446–453 (2013).



33. Hoa, N. D. *et al.* Nanowire structured SnO_x-SWNT composites: High performance sensor for NO_x detection. *Sens. Actuators B: Chem.* **142**, 253–259 (2009).
34. Sayago, I. *et al.* The effect of additives in tin oxide on the sensitivity and selectivity to NO_x and CO. *Sens. Actuators B: Chem.* **26–27**, 19–23 (1995).
35. Lin, C. Y. *et al.* Fabrication of NO_x gas sensors using In₂O₃-ZnO composite films. *Sens. Actuators B: Chem.* **146**, 28–34 (2010).
36. Epifani, M. *et al.* The role of surface oxygen vacancies in the NO₂ sensing properties of SnO₂ nanocrystals. *J. Phys. Chem. C* **112**, 19540–19546 (2008).
37. Maiti, A. *et al.* SnO₂ nanoribbons as NO₂ sensors: insights from first principles calculations. *Nano Lett.* **3**, 1025–1028 (2003).
38. Fan, F. Y. *et al.* Synthesis and gas sensing properties to NO₂ of ZnO nanoparticles. *Sens. Actuat. B-Chem.* **185**, 377–382 (2013).

Acknowledgments

This work was supported by the National Natural Science Foundation of China (Grant No. 21103046, 21373081, 51302079 and 61376073) and the Young Teachers' Growth Plan of Hunan University (Grant No. 2012-118).

Author contributions

J.M.M., Z.X. and T.H.W. proposed and designed the experiments. L.W. and Y.J.C. carried out the synthetic experiments and conducted the characterization. L.W., Y.J.C. and L.B.C. performed the HRTEM, SEM characterization and structural analysis. L.W. and Q.H.L. analysed the data. L.W., J.M.M., Z.X. and T.H.W. wrote the manuscript. All the authors participated in discussions of the research.

Additional information

Supplementary information accompanies this paper at <http://www.nature.com/scientificreports>

Competing financial interests: The authors declare no competing financial interests.

How to cite this article: Wang, L. *et al.* Hierarchical SnO₂ Nanospheres: Bio-inspired Mineralization, Vulcanization, Oxidation Techniques, and the Application for NO Sensors. *Sci. Rep.* **3**, 3500; DOI:10.1038/srep03500 (2013).



This work is licensed under a Creative Commons Attribution-NonCommercial-ShareAlike 3.0 Unported license. To view a copy of this license, visit <http://creativecommons.org/licenses/by-nc-sa/3.0>